Optical properties of imperfect strained-layer InAs/$Ga_{1-x}In_xSb$/AlSb superlattices with infrared applications

M. R. Kitchin,* M. J. Shaw, E. Corbin, J. P. Hagon, and M. Jaros
Department of Physics, The University of Newcastle upon Tyne, Newcastle upon Tyne, NE1 7RU, United Kingdom
(Received 22 July 1999; revised manuscript received 4 October 1999)

We present a microscopic model of the optical properties of several strained-layer InAs/GaSb-based superlattice structures with infrared optoelectronic applications. The requirements, both in technologically motivated and basic physics, for improvements in the theory of the optical properties of disordered, strained-layer systems are identified. Both disordered and perfect structures are modeled, and we analyze in detail their optical spectra, identifying the role played by wave-function confinement in determining spectral features. For those structures with laser applications, we study in detail the effect of alloy layer disorder on emission line shape at various population inversions. We find that there is a significant change in the linewidth as a result of alloy layer disorder. The optical absorption of a photodetector structure is modeled, and we appraise the potentially degrading effects of Auger recombination processes on its operation. We find good agreement between our predictions and experimental results. This paper presents a set of results in an ongoing research program in which we aim to gain a quantititative understanding of the relationship between microscopic disorder and strain and the optical properties of semiconductor heterostructures.

I. INTRODUCTION

Antimonide-based heterostructures exhibiting optical spectra in the infrared have been successfully fabricated since the late 1980s.[1] These so-called ''6.1-Å'' heterostructures are composed from antimonides and other III-V semiconductors with lattice constants of around this value, such as GaSb, AlSb, and InAs. Flexibility in the design of these structures is further accommodated by alloying these materials with each other or with less well lattice-matched InSb. The materials, layer thicknesses, and alloy and strain configurations used in these systems function as design parameters in engineering the electronic band structure to give fine-tuned optical properties in the far-infrared. In consequence, such structures demonstrate huge potential in optoelectronic applications as IR photodetectors[2–6] and lasers.[7–11] The value of these materials in such applications is well documented in the literature,[12] and includes features such as deep wells exhibiting high carrier mobilities and type-II band lineups with fundamental gaps in the infrared. However, at present practical application of antimonide heterostructures is limited by the lifetimes which can be achieved by current growth methods. Scanning tunneling-electron microscopy techniques have facilitated a direct determination of the specific microscopic disorder configurations arising in these heterostructures,[13–15] enabling appraisals of interfacial quality to be carried out. A quantitative understanding of the effects of both microscopic disorder and strain fields on the optical line shapes of these structures is of principal importance in the design of devices. Indeed, recent studies using *ab initio* pseudopotential calculations showed that the microscopic interaction between defects and the interfacial bonds can play a significant role in determining the properties of defects in heterostructures.[16,17] In particular, one of the key problems for theoretical models is to provide an adequate description of the microscopic configuration of alloy layers. If antimonide-based technology is to become widespread in the fields of these applications, a detailed understanding of the microscopic features which determine device performance is required so that structures may be optimized to achieve particular response characteristics.

In this paper, we report large-scale calculations of the optical spectra of both ideal and imperfect antimonide-based superlattices with optoelectronic applications. We employ an empirical pseudopotential scheme incorporating strain effects and enabling band-structure calculations in multilayer superlattices containing microscopic disorder, including that associated with alloy layers. For two laser structures, each incorporating $Ga_{1-x}In_xSb$ alloy layers, we examine the effect of the microscopic alloy configuration upon the emission spectra, in particular the effect on the emission linewidth. In addition, we model a detector structure which does not contain an alloy layer, and present the absorption spectrum arising from a calculation of the ideal superlattice band structure. We give a comparison between the features of this latter result and an experimentally obtained spectrum for this structure,[18] appraising its performance as an IR detector. These calculations provide us with an essential insight into the microscopic physical processes governing the optical characteristics of the structures.

II. DETAILS OF CALCULATION

We calculate the stationary-state solutions in perfect (that is, assuming no disorder) superlattice structures using the empirical pseudopotential method,[19] which was originally developed to calculate the electronic band structure in bulk crystalline materials.[20] The presence of biaxial strain fields in heterostructures, arising from lattice mismatch, requires an evaluation of strained superlattice potentials, and we delineate the method of determining these elsewhere.[21] Strained band offsets, between the constituent materials, are evaluated using the method of Van de Walle.[22]

To additionally model disorder in such systems, we define a larger unit cell, comprising many superlattice primitive cells, and can apply disorder throughout specific layers in this so-called supercell. The disorder potential is treated as a perturbation on the ideal superlattice potential, and the eigenfunctions of this perturbed system are expanded in a basis of the wave functions of the ideal superlattice.[21,23] In alloy materials, the microscopic potential is conventionally modeled using the virtual crystal (VC) approximation[24] by taking a weighted average of the potentials of the constituents at the correct fractions. Our approach facilitates a more realistic alloy model in which the potential may be represented as a spatially disordered configuration of the constituents, without averaging: the atomic pseudopotentials of the species in the alloy layer are randomly distributed between the atom sites, to the correct fractions. For such calculations, it is convenient to perform an idealized calculation using the VC potential, and to carry out subsequent disorder calculations as perturbations. We take account of atomic relaxation in disordered systems by utilizing a valence force field method.

Previous studies[25] indicated that, in order to model the detailed optical response of a nanostructure, it is necessary to sample a large number of k points in the Brillouin zone. However, following examination of the electronic band structure along various symmetry directions in the Brillouin zone, the region of k space to sample may be chosen such that only transitions in the energy range of interest are considered. For an optical-absorption calculation, a large energy range would be required in order to study the optical response for a wide frequency range of incident radiation. In such a case, a fairly large volume of k space is likely to be necessitated. If, on the other hand, an emission spectrum is to be computed, the calculation will generally involve a far smaller range in energy (and hence in k space), which is dictated by the fundamental gap and the Fermi surface. By carrying out the preliminary calculations described, we avoid wasteful computation in the subsequent sampling. In the case of an ideal superlattice, the sampling region lies within one irreducible segment of the Brillouin zone.[26] For disordered structures, in which the point-group symmetry of the unit cell is broken and only time-reversal symmetry remains, the sampling region necessarily covers a greater fraction of the zone.

The microscopic relationship between the optical properties of a system and its band structure is well documented in the literature.[25,27] Emission processes are characterized by the linear susceptibility $\chi^{(1)}$,[25] whereas absorption processes are described in terms of the linear absorption coefficient $\alpha(\omega)$, which is related to $\chi^{(1)}$ by

$$\alpha(\omega)=\frac{\omega}{n_0 c}\mathrm{Im}[\chi^{(1)}(-\omega;\omega)]. \tag{1}$$

Here c is the speed of light in a vacuum, and n_0 is the background refractive index resulting from electrons in the ion cores.

In the case of an absorption calculation, the optical sum appearing in the linear susceptibility expression[25] includes all direct interband transitions for the minibands of interest. For an emission calculation, the set is restricted to those direct conduction-to-valence-band transitions permissible for a particular population inversion. We utilize the linear-analytic method of zone integration,[28] for our grid of sampling points, to generate smooth, linearly interpolated curves for the optical spectra and density of states.

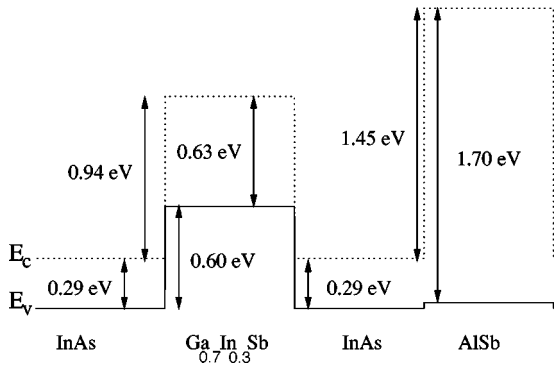

FIG. 1. Band offset diagram for the strained-layer $6\mathrm{InAs}/10\mathrm{Ga}_{0.7}\mathrm{In}_{0.3}\mathrm{Sb}/6\mathrm{InAs}/14\mathrm{AlSb}$ superlattice, calculated using the method of Van de Walle (Ref. 22). Band-gap energies are given in eV.

III. RESULTS

In this section, we present the results of optical spectra calculations for several superlattice systems having IR technological applications. By considering zone-center wavefunction confinement effects for states close to the band edges, we interpret various features of these spectra. We model the linear susceptibility characterizing emission processes in those structures which have laser applications and an investigation into the effects of alloy layer disorder on the optical line shape is reported. Optical absorption is calculated for a structure having an application as a photodetector and the likelihood of Auger recombination processes arising in this device assessed. Furthermore, where experimental data are available, we utilize this to exemplify the success of our method in modeling such structures.

A. Infrared laser applications: Emission

The electronic band-structure and emission spectra of a $6\mathrm{InAs}/10\mathrm{Ga}_{0.7}\mathrm{In}_{0.3}\mathrm{Sb}/6\mathrm{InAs}/14\mathrm{AlSb}$ superlattice, which we assume to be pseudomorphically strained to its AlSb buffer layer, have been modeled. The aim of these calculations was to study the way in which atomic disorder in the $\mathrm{Ga}_{1-x}\mathrm{In}_x\mathrm{Sb}$ alloy layer affects the line shape of the linear susceptibility which characterizes these emission processes. This superlattice has been grown by Yang *et al.*[29] for the active region of an IR quantum cascade laser. To assist an investigation of the likely carrier confinement in this heterostructure, Fig. 1 illustrates its strained layer band offsets. Here E_v and E_c are the zone-center energies of the highest valence and lowest conduction bands, respectively, in the strained bulk materials. As the diagram indicates, the InAs and alloy layers form a type-II misaligned (or broken gap) band lineup, whereas the InAs and AlSb have a type-II staggered lineup. The structure is that of a so-called W laser in which the AlSb conduction-band edges form large barriers to the InAs quantum wells (QW's), the latter being separated by the small alloy layer barriers. In the valence band, holes are confined

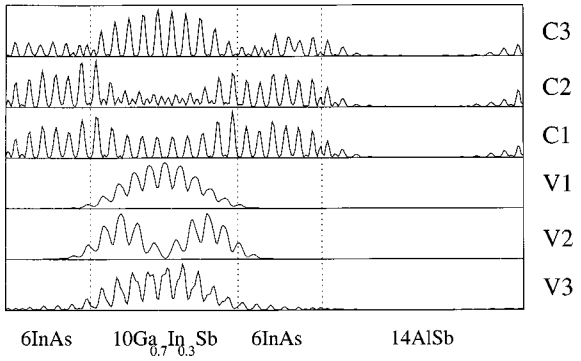

FIG. 2. Zone-center charge densities for the $6InAs/10Ga_{0.7}In_{0.3}Sb/6InAs/14AlSb$ superlattice, plotted along the growth direction, down the atomic spiral center, for a virtual-crystal alloy potential. The states depicted correspond to the top three valence ($V1$, $V2$, and $V3$) and lowest three conduction ($C1$, $C2$, and $C3$) miniband pairs.

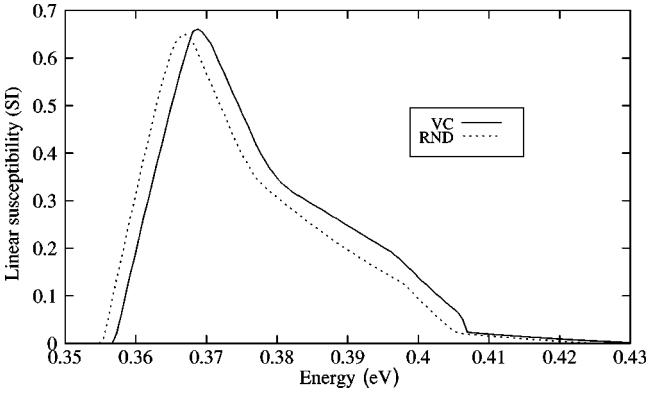

FIG. 3. Normal (x polarization) incidence emission spectra [linear susceptibility (SI) vs photon energy (eV)] for the superlattice represented in Figs. 1 and 2, for the virtual-crystal (VC) and random (RND) alloy potentials. The carrier concentration is 3.2×10^{16} cm^{-3}.

in the alloy layer QW's, with the InAs, and to a lesser extent AlSb, layers forming barriers. Since the lowest bulk InAs conduction band is lower in energy than the highest bulk valence band in the alloy, the fundamental band gap of the superlattice may be smaller than that in any of the constituent bulk materials. Such structures facilitate high-wavelength interband transitions and may prove useful in IR applications if a high degree of electron and hole wave-function overlap is exhibited for states close to the band edges.

In order to investigate carrier confinement in the potential profile described further, Fig. 2 depicts the zone-center wave functions for the top three valence (V) and lowest three conduction (C) spin-degenerate pairs of minibands, as determined from the band structure calculated. This figure indicates distinct confinement of holes in the valence band QW, in the alloy layer, with only small charge leakage to the InAs barriers. For conduction states, however, the electron wave functions exhibit a high degree of tunneling from the InAs wells into the alloy barriers. While Fig. 1 shows that the conduction well is actually deeper than the corresponding valence well, suggesting that confinement should be greater in the conduction band, this phenomenon is not observed: the conduction band has a lower effective mass, permitting wave-function tunneling, which leads to the relatively unconfined states observed. However, Fig. 2 also indicates that electron tunneling to the larger and thicker AlSb barriers is minimal.

Since the fundamental gap of this superlattice corresponds to transitions across the type II misaligned interface between the InAs and alloy layers, high transition probabilities are anticipated because the interband wave-function overlap is large across this heterojunction. Furthermore, because the alloy layer forms one side of this key interface, we anticipate that the microscopic detail of the alloy potential will have a significant influence on the energies and strengths of these interband optical transitions. In the forthcoming figures, spectra labeled VC were calculated using the virtual crystal approximation for the $Ga_{1-x}In_xSb$ alloy layer model. Those spectra denoted RND result from perturbation calculations, in which a random cation distribution was modeled in the alloy layer. To achieve this, a perturbation potential is used in which each VC cation potential, within one lattice constant from the interfaces with the InAs layers, is randomly substituted with the cation potentials of either GaSb or InSb, in the correct fractions. As such, the spatial and compositional averaging of the VC alloy potential model is replaced with a more realistic form close to the heterointerfaces, accounting for random disorder.

Figure 3 exhibits emission spectra for light propagating in the direction normal to the interfacial planes of the superlattice, such that the electric-field vector is polarized in the x (in-plane) direction. These spectra were calculated for an excited carrier population of 3.2×10^{16} cm^{-3}, the concentration of electrons excited to the conduction band and holes present in the valence band. It is clear that the linear susceptibilities calculated using the two alloy layer models differ regarding the fine structure of the spectra. However, the line shapes close to the cutoff are largely unchanged apart from a small redshift of around 2 meV exhibited by the RND spectrum relative to the VC case. Modeling disorder in the alloy layer does not lead to line-shape broadening, relative to the simplistic VC model, and we do not anticipate a large change in device performance based on the effects of disorder on carrier lifetimes, from this polarization.

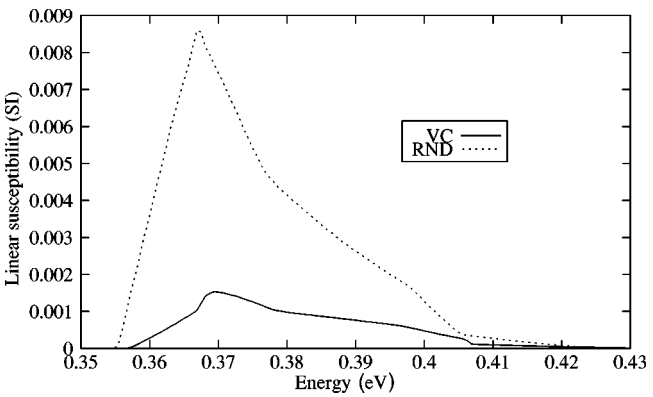

FIG. 4. Parallel (z polarization) incidence emission spectra [linear susceptibility (SI) vs photon energy (eV)] for the superlattice represented in Figs. 1 and 2, for the virtual-crystal (VC) and random (RND) alloy potentials. The carrier concentration is 3.2×10^{16} cm^{-3}.

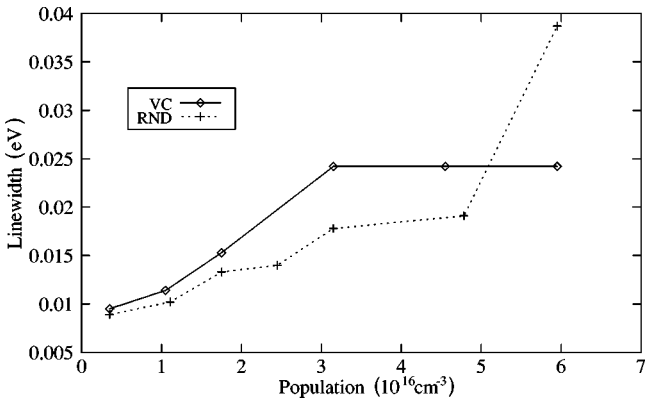

FIG. 5. Linewidth (eV) vs carrier concentration (cm^{-3}) for both the RND and VC alloy potentials, for the superlattice represented in Figs. 1 and 2.

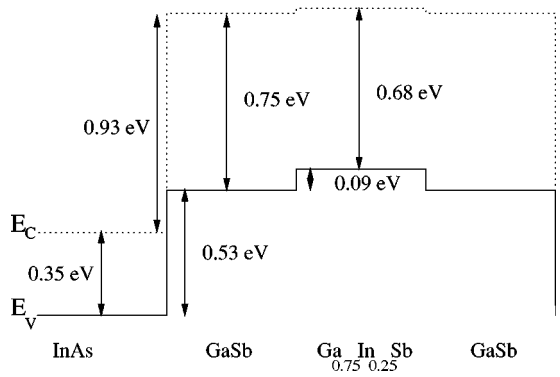

FIG. 6. Band-offset diagram for the strained-layer 4InAs/4GaSb/2$Ga_{0.75}In_{0.25}$Sb/4GaSb superlattice, calculated using the method of Van de Walle (Ref. 22). Band-gap energies are given in eV.

Figure 4 shows the corresponding emission spectra obtained for light propagating parallel to the superlattice interfacial planes, for which the electric field vector is polarized along the superlattice growth direction *z*. The spectra obtained with the VC and RND models exhibit significantly different line shapes for this polarization, the susceptibilities being clearly greater with the RND potential. To assess the effect of this disorder configuration on line shape more generally, we consider broadening effects as a function of the excited carrier population. Figure 5 depicts the linewidths (energy spread of line shape at half maximum) obtained using both the VC and RND alloy layer models, plotted against the population. The linewidth is seen to increase with carrier density, as is expected, due to population of progressively higher-energy states with electrons, the corresponding increase in holes in the valence band and the transitions which this facilitates. For both alloy layer models, the linewidth appears to level off to a plateau at around 3.2×10^{16} cm^{-3}. This effect derives from the complete population of those states in the first miniband $C1$ having strong transition probabilities. While more energetic states are filled with increasing population, these do not make a large contribution to the spectrum, and hence the linewidth does not increase until higher conduction (lower valence) states leading to large transition strengths are populated (emptied). At higher carrier concentrations (not depicted), the linewidth changes dramatically, due to the onset of $C2$ (the second conduction miniband) population and the transitions which this facilitates.

Figure 5 indicates that, for a given carrier concentration, the linewidth is generally greater for the VC potential than for that of the RND case. This is rather surprising as it is generally the case that disorder leads to line-broadening in semiconductors. However, the reduced linewidth exhibited by the RND case arises from changes to the electronic band structure, namely, a reduction in band dispersion, as opposed to a change in carrier lifetimes. The comparison in Fig. 5 shows that the linewidth is significantly reduced, by up to around ~10 meV, due to inclusion of the RND configuration, at populations below 5.0×10^{16} cm^{-3}. To our knowledge, no experimental spectral data are available at present for these structures, which would allow us to distinguish between the line shapes arising from different disorder configurations. Furthermore, we note that the STM measurements discussed earlier have shown that atomic reordering processes, namely, surface/interfacial reconstruction, can arise in semiconductor heterostructures.[13] As consequence, while we have modeled atomistic disorder in the alloy layer of this structure, the actual configurations arising in these superlattices may manifest some degree of reordering, and will be the subject of a further study.

An investigation of emission in an antimonide-based superlattice containing an alloy layer which does not form part of the key type-II interface is now reported. This study was carried out in an attempt to identify the influence of disorder present in such an alloy layer on the optical line shape. This structure, a 4InAs/4GaSb/2$Ga_{0.75}In_{0.25}$Sb/4GaSb superlattice, was fabricated for the active region of a 2.9-μm diode laser by Bewley *et al.*[30] In order to identify the key interface for interband transitions and the anticipated carrier confinement, Figure 6 illustrates the superlattice band offsets, assuming pseudomorphic strain to the [100] GaSb substrate. As the diagram indicates, the InAs and GaSb layers form a type-II misaligned (or broken gap) band lineup, whereas the GaSb and alloy have a small type-II staggered lineup. The alloy and GaSb layers act as a barrier to electrons in the conduction band and a well to holes in the valence band. Thus, the key type-II interface for interband optical transitions is the InAs/GaSb heterojunction for this structure. We depict zone-center superlattice wave functions for such states in Fig. 7, for near-band-edge states. This figure indicates that valence states are mainly confined to the alloy/GaSb well, close to the band edge. Conduction state confinement is less distinct, the charge density being significant in magnitude throughout the structure. While the conduction well is deeper than the corresponding valence well, suggesting that conduction-band confinement should be greater, this phenomenon is not observed. The charge leakage is again attributed to the lower conduction-band effective mass, in addition to a narrower barrier, which permit wave function tunneling and lead to the relatively unconfined states observed. We note, however, that in the alloy conduction barrier the amplitude of these charge densities are generally small. Due to the significant conduction-valence wave-function overlap in the GaSb and alloy layers, we anticipate large optical transition strengths between these band-edge states.

The linear susceptibility characterizing the emission processes was evaluated as for the previous structure. Again,

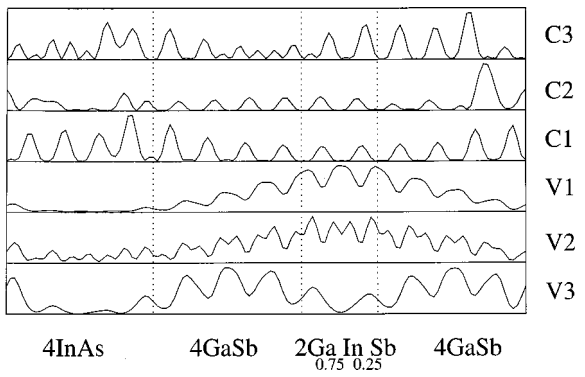

FIG. 7. Zone-center charge densities for the 4InAs/4GaSb/$2Ga_{0.75}In_{0.25}Sb$/4GaSb superlattice, plotted along the growth direction, down the atomic spiral center, for a virtual-crystal alloy potential. The states depicted correspond to the top three valence ($V1$, $V2$, and $V3$) and lowest three conduction ($C1$, $C2$, and $C3$) miniband pairs.

calculations were performed using both the VC and RND alloy models. Both polarizations exhibit an emission cutoff at 527 meV which corresponds to the fundamental band gap and is equivalent to a cutoff wavelength of 2.4 μm. This result is in good agreement with the experimental value[30] of 2.9 μm. As for the previous superlattice, the *x*-polarization spectra calculated using these two alloy models were very similar. However, the results additionally showed that the *z*-polarization spectra predicted with the VC and RND alloy models were very similar to each other for this superlattice, unlike the corresponding spectra for the previous heterostructure. Figure 8 depicts an example of these *z*-polarized spectra for an excited carrier population of 1.7×10^{16} cm^{-3}. It is clear from the figure that the two line shapes are very similar, with little indication of broadening effects. As was identified earlier, the InAs/GaSb heterojunction is the key interface for interband transitions in this superlattice. As a consequence, the specific detail of the alloy layer configuration is unlikely to have a large effect on the susceptibility in this structure, as the results indeed indicate. Accordingly, the simplistic VC model, which does not describe alloy layer disorder, appears to represent an adequate approximation to the alloy layer potential, in modeling emission for the present superlattice.

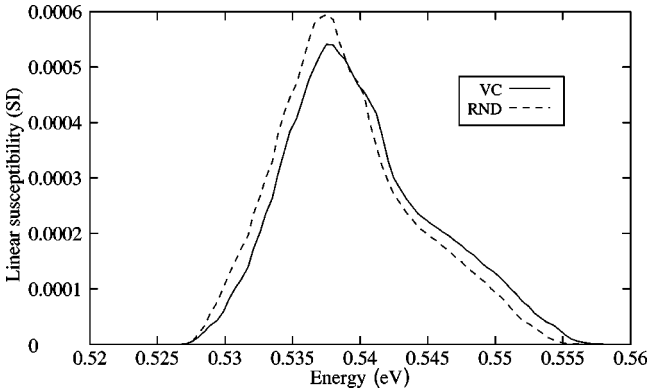

FIG. 8. Parallel (*z* polarization) incidence emission spectra [linear susceptibility (SI) vs photon energy (eV)] for the superlattice represented in Figs. 6 and 7, for both the virtual-crystal (VC) and random (RND) alloy potentials, and for a carrier density of 1.7×10^{16} cm^{-3}.

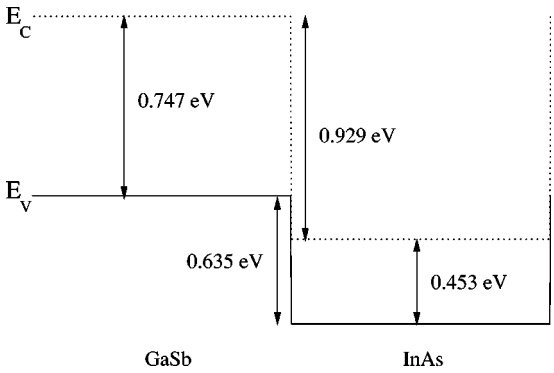

FIG. 9. Band-offset diagram for the strained-layer 16InAs/16GaSb superlattice, calculated using the method of Van de Walle (Ref. 22). Band-gap energies are given in eV.

B. Infrared detector applications: Absorption

In this section we model IR absorption in a perfect (disorder-free) 16InAs/16GaSb superlattice strained to a GaSb buffer layer. This structure was recently grown by Mohseni *et al.*[18] for application as a type-II infrared photodetector. A 125 *k*-point grid was sampled for the calculation, and the range of bands to include in the optical sum appearing in the absorption coefficient expression was chosen such that all interband transitions $\leqslant$500 meV were considered. Figure 9 depicts the valence- and conduction-band offsets assuming pseudomorphic straining to the GaSb buffer. The type-II misaligned lineup again leads to superlattice states giving interband transitions with energies smaller than either of the bulk band gaps, and as such is potentially useful for long-wavelength applications. That these wavelengths lie in the infrared is to be predicted by the band structure and absorption calculation, though first we consider the likely transition strengths which, as in the preceding emission calculations, are governed by the overlap of wave functions between the electron and hole states.

Figure 10 depicts the zone-center charge densities for the top three valence and bottom three conduction spin-

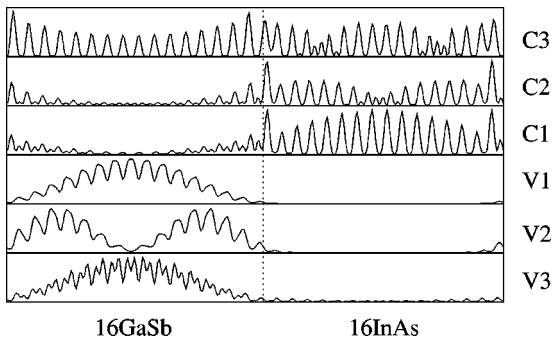

FIG. 10. Zone-center charge densities for the 16InAs/16GaSb superlattice, plotted along the growth direction, down the atomic spiral center. The states depicted correspond to the top three valence ($V1$, $V2$, and $V3$) and lowest 3 conduction (C1, C2, C3) miniband pairs.

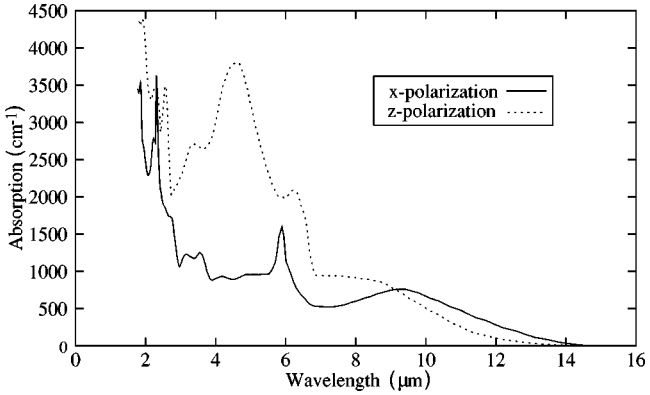

FIG. 11. Normal (x polarization) and parallel (z polarization) incidence absorption spectra [linear absorption coefficient (cm^{-1}) vs photon wavelength (μm)] for the superlattice represented in Figs. 9 and 10.

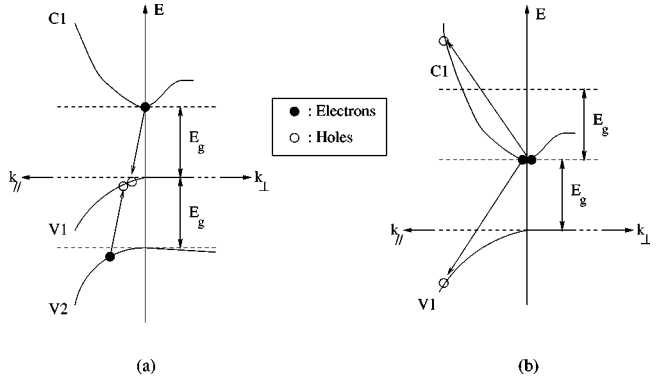

FIG. 12. Schematic diagram of the (a) AM-7 hole-hole (Refs. 34 and 35) and (b) AM-1 electron-electron (Ref. 34) Auger recombination processes.

degenerate miniband pairs. The hole states show large confinement to the GaSb valence well, though a slight charge leakage to the InAs barriers is exhibited. Similarly, the electron wave functions are largest in the InAs conduction well, though in this case a significant amount of tunneling to the GaSb barriers is observed due to the lighter conduction-band effective mass. Thus wave-function overlap is good close to the heterojunctions, suggesting cross-interface transition strengths suitable for interband optical devices.

Figure 11 depicts the normal (x-polarized) and parallel (z-polarized) incidence absorption spectra for transitions up to 500 meV in energy, which corresponds to a range of wavelengths from the cutoff down to around 2.5 μm. We plot the curves as a function of wavelength, rather than energy, to adhere to the convention for the absorption spectra of detectors and thus to ease comparison with the experimental results cited earlier. While emission spectra, such as those considered earlier in this paper, indicate the detail of the band structure over a small energy range, absorption processes involve direct transitions over a far larger range of energies and hence of momentum space and miniband indices. As such, this calculation requires a broader view of band-structure features, and illustrates a different, use of the model. Comparison with the experimental results[18] indicates good agreement in the cutoff wavelength at around 14 μm. The x-polarization spectrum exhibits a dip at around 7 μm which is also distinct on the experimental spectrum. The x-polarization again dips below a peak at around 6 μm, whereas the z-polarization spectrum rises significantly in this region. The latter resembles the experimental results most closely, as this spectrum also rises dramatically below 7 μm. Significantly, the experimental spectrum was measured at the Brewster angle to the direction of incident light, and as such will contain contributions from both polarizations, as we indeed observe from comparison with our calculation. The agreement with these experimental results provides further evidence in support of our model for optical spectra.

Nonradiative recombination processes degrade the performance of optoelectronic applications, since these may deplete bands of carriers which could potentially participate in optical transitions. Full band structure calculations of the Auger rate, which account for processes throughout the entire Brillouin zone, were previously carried out for $Si/Si_{1-x}Ge_x$ multiple-quantum-well (MQW) systems by our Research Group.[31–33] While such calculations lie beyond the scope of this paper and require large computation times, it is possible to glean a good indication of the overall Auger recombination rates from considerations of the zone center energy-band separations.[34,35] In the case of long-wavelength superlattice infrared detectors it is advantageous to suppress hole-hole Auger recombination processes, which reduce the excited electron concentration in conduction states. Such a process, termed AM-7 in the literature,[34] is illustrated in Fig. 12(a). The AM-7 process may be suppressed by engineering the top two valence bands to be separated by an energy greater than the fundamental gap.[35] Examination of the detector band structure (not depicted) indicates that the fundamental gap $E_g = 0.084$ eV, whereas the separation of the highest two pairs of valence minibands, $V1$ and $V2$, is equal to 0.097 eV at Γ. Thus, it is anticipated that this design suppresses the AM-7 Auger process, making it useful for application as an IR detector.

Electron-electron Auger processes may also be important, the most important example being deemed to be the AM-1 case in the literature.[34] This process is depicted schematically in Fig. 12(b). By engineering the width of the lowest conduction band ($C1$) in the growth direction $k_\perp$, such that it is smaller than the fundamental gap, AM-1 recombination may be suppressed. While these processes may still take place along $k_\parallel$, they would scatter electrons into valence states remote from Γ, which have small hole concentrations and hence should not constitute a large nonradiative recombination rate. Further examination of the detector band structure shows that the width of the $C1$ miniband (from Γ to P, the growth direction Brillouin-zone boundary) is 0.030 eV, which is indeed less than E_g. In consequence, the device is expected to be successful in suppressing AM-1 Auger recombination.

IV. CONCLUSIONS

In this paper, we have identified the demand, both within technological and basic physics, for improvements in the theory of microsopic disorder and strain with respect to the optical properties of heterostructures. We delineated a model of the optical line shapes of such systems which facilitates an

atomistic description of the microscopic alloy potential, lattice relaxation at defect sites, and biaxial strain. The emission spectra of a number of type-II laser structures were considered, each showing significant infrared emission, as is consistent with the wave-function overlap of band edge states. We modeled randomly disordered cation potentials in the alloy layers of each superlattice, and compared to the results for a virtual crystal (VC) alloy layer potential. We find that accounting for microscopic disorder leads to a significant change in the optical linewidth, compared to the result obtained using the VC approximation, for structures in which the alloy layer forms part of the type-II interface. Our analysis shows that this broadening arises from changes to the electronic band structure.

In assessing the optical absorption characteristics of a detector device, we predict significant wave-function overlap, leading to a strong infrared optical response. The cutoff wavelength and general lineshape features of the calculated spectra are in good agreement with those recently obtained by experiment. Furthermore, we find that the principal zone-center Auger recombination processes which are deemed to degrade the performance of such devices are successfully suppressed for the detector structure.

In this paper, our microscopic model of imperfect heterostructures has been applied to the particular case of random disorder in the alloy layers of antimonide-based systems. However, there may be more general applications in the study of microscopic ordering in alloys in addition to other key topics in device physics, such as interfacial disorder, reconstruction effects, and the description of substitutional impurities. This method provides a valuable quantitative link between the microscopic features of heterostructures and the macroscopic properties which govern their performance as devices.

ACKNOWLEDGMENTS

We would like to thank the U.S. Office of Naval Research and D.E.R.A. (Malvern) for financial support.

*Author to whom correspondence should be addressed. FAX: +44 191 2227361. Electronic address: m.r.kitchin@ncl.ac.uk

[1] D.L. Smith, and C. Mailhiot, J. Appl. Phys. **62**, 2545 (1987).
[2] M.H. Young, D.H. Chow, A.T. Hunter, and R.H. Miles, Appl. Surf. Sci. **128**, 395 (1998).
[3] J.L. Johnson, L.A. Samoska, A.C. Goddard, J.L. Mertz, M.D. Jack, G.R. Chapman, B.A. Baumgratz, K. Kosai, and S.M. Johnson, J. Appl. Phys. **80**, 1116 (1996).
[4] F. Szmulowicz, E.R. Heller, K. Fisher, and F.L. Madarasz, Superlatt. Microstruct. **17**, 373 (1995).
[5] I.H. Campbell, I. Sela, B. K Laurich, D.L. Smith, C.R. Bolognesi, L.A. Samoska, A.C. Gossard, and H. Kroemer, Appl. Phys. Lett. **59**, 846 (1991).
[6] D.H. Chow, R.H. Miles, J.R. Söderström, and T.C. McGill, Appl. Phys. Lett. **56**, 1418 (1990).
[7] L.J. Olafsen, E.H. Aifer, I. Vurgaftman, W.W. Bewley, C.L. Felix, J.R. Meyer, D. Zhang, C.-H. Lin, and S.S. Pei, Appl. Phys. Lett. **72**, 2370 (1998).
[8] J.R. Meyer, L.J. Olafsen, E.H. Aifer, W.W. Bewley, C.L. Felix, I. Vurgaftman, M.J. Yang, L. Goldberg, D. Zhang, C.-H. Lin, S.S. Pei, and D.H. Chow, IEE Proc.: Optoelectron. **145**, 275 (1998).
[9] I. Vurgaftman, J.R. Meyer, and L.R. Ram-Mohan, IEEE J. Quantum Electron. **34**, 147 (1998).
[10] R.M. Biefield, A.A. Allerman, and S.R. Kurtz, Mater. Sci. Eng., B **51**, 1 (1998).
[11] H.Q. Lei, C.H. Lin, and S.S. Pei, Appl. Phys. Lett. **72**, 3434 (1998).
[12] J. Wagner, J. Schmitz, F. Fuchs, J.D. Ralston, P. Koidl, and D. Richards, Phys. Rev. B **51**, 9786 (1995).
[13] B.Z. Nosho, W.H. Weinberg, J.J. Zinck, B.V. Shanabrook, B.R. Bennett, and L.J. Whitman, J. Vac. Sci. Technol. B **16**, 2381 (1998).
[14] J. Harper, M. Weimer, D. Zhang, C.-H. Lin, and S.S. Pei, Appl. Phys. Lett. **73**, 2805 (1998).
[15] J. Harper, M. Weimer, D. Zhang, C.-H. Lin, and S.S. Pei, J. Vac. Sci. Technol. B **16**, 1389 (1998).
[16] M.J. Shaw, P.R. Briddon, and M. Jaros, Phys. Rev. B **54**, 16 781 (1996).
[17] M.J. Shaw, Phys. Rev. B **58**, 7834 (1998).
[18] H. Mohseni, E. Michel, Jan Sandoen, M. Razeghi, W. Mitchel, and G. Brown, Appl. Phys. Lett. **71**, 1403 (1997).
[19] See, e.g., M.A. Gell, D. Ninno, M. Jaros, and D.C. Herbert, Phys. Rev. B **34**, 2416 (1986).
[20] J.R. Chelikowsky and M.L. Cohen, Phys. Rev. B **14**, 789 (1976).
[21] M. J. Shaw, Phys. Rev. B **61**, 5431 (2000).
[22] C.G. Van de Walle, Phys. Rev. B **39**, 1871 (1989).
[23] C. Jenner, E. Corbin, B.M. Adderley, and M. Jaros, Semicond. Sci. Technol. **13**, 359 (1998).
[24] M. Jaros, Rep. Prog. Phys. **48**, 1091 (1985).
[25] M.J. Shaw, M. Jaros, Z. Xu, P.M. Fauchet, C.W. Rella, B.A. Richman, H.A. Schwettman, and G.W. Wicks, Phys. Rev. B **50**, 18 395 (1994).
[26] C.J. Bradley and A.P. Cracknell, *The Mathematical Theory of Symmetry in Solids* (Clarendon Press, Oxford, 1972).
[27] F. Bassani and G. Pastori Parravicini, *Electronic States and Optical Transitions in Solids* (Pergamon Press, Oxford, 1975).
[28] P.E. Blöchl, O. Jepsen, and O.K. Andersen, Phys. Rev. B **49**, 16 223 (1994).
[29] M.J. Yang, W.J. Moore, B.R. Bennett, and B.V. Shanabrook, Electron. Lett. **34**, 270 (1998).
[30] W.W. Bewley, E.H. Aifer, C.L. Felix, I. Vurgaftman, J.R. Meyer, C.-H. Lin, S.J. Murry, D. Zhang, and S.S. Pei, Appl. Phys. Lett. **71**, 3607 (1997).
[31] K.B. Wong, G.K.A. Gopir, J.P. Hagon, and M. Jaros, Semicond. Sci. Technol. **9**, 2210 (1994).
[32] E. Corbin, C.J. Williams, K.B. Wong, R.J. Turton, and M. Jaros, Superlatt. Microstruct. **19**, 25 (1996).
[33] C.J. Williams, E. Corbin, M. Jaros, and D.C. Herbert, Physica B **254**, 240 (1998).
[34] M.E. Flatté, C.H. Grein, H. Ehrenreich, R.H. Miles, and H. Cruz, J. Appl. Phys. **78**, 4552 (1995).
[35] C.H. Grein, P.M. Young, and H. Ehrenreich, Appl. Phys. Lett. **61**, 2905 (1992).